Degradation of radar reflectivity by cloud attenuation at microwave frequency

Olivier Pujol, Jean-François Georgis, Laurent Féral, Henri Sauvageot

Degradation of Radar Reflectivity by Cloud Attenuation at Microwave Frequency

OLIVIER PUJOL AND JEAN-FRANÇOIS GEORGIS

Laboratoire d'Aérologie, Observatoire Midi-Pyrénées, Université Paul Sabatier, Toulouse, France

LAURENT FÉRAL

Laboratoire AD2M, Université Paul Sabatier, Toulouse, France

HENRI SAUVAGEOT

Laboratoire d'Aérologie, Observatoire Midi-Pyrénées, Université Paul Sabatier, Toulouse, France

(Manuscript received 2 November 2005, in final form 7 June 2006)

ABSTRACT

The main object of this paper is to emphasize that clouds—the nonprecipitating component of condensed atmospheric water—can produce a strong attenuation at operational microwave frequencies, although they present a low reflectivity preventing their radar detection. By way of a simple and realistic model, simulations of radar observations through warm precipitating targets are thus presented in order to quantify cloud attenuation. Simulations concern an airborne radar oriented downward and observing precipitation at four frequencies: 3, 10, 35, and 94 GHz. Two cases are first considered: a convective cell (vigorous cumulus congestus plus rain) and a stratiform one (nimbostratus plus drizzle) superimposed on the previous one. Other simulations are then performed on different types of cumulus (congestus, mediocris, and humilis) with various thicknesses characterized, in a microphysical sense, by their maximum liquid water content.

Simulations confirm the low cumulus reflectivity ranging from −45 dBZ for the weakest cumulus (i.e., the humilis one) to −5 dBZ for the strongest one (i.e., the vigorous cumulus congestus). It reaches −35 dBZ for the nimbostratus cloud. On the other hand, cumulus attenuation [precisely path-integrated cloud attenuation (PICA)] is not negligible and, depending on the frequency, can be very strong: the higher the frequency, the stronger the PICA. At 3 GHz, the far less attenuated frequency, PICA for the vigorous cumulus congestus alone in the convective cell (embedded into the stratiform background) is on the order of 1.2 dB (1.5 dB) at 10 GHz, 16 dB (20 dB) at 35 GHz, and 80 dB (100 dB) at 94 GHz. For weaker cumulus, PICA is lower but, in certain cases, significant. All these results mean that it is necessary to be very careful about radar measurements if reliable information on precipitation—for example, the precipitation rate R—has to be deduced, particularly at high operational frequencies.

1. Introduction

Radar meteorology uses backscattering by hydrometeors to assess, via the measured radar reflectivity factor Z_m, various physical characteristics of clouds and precipitation, such as precipitation rate (R), water content (M), or hydrometeors' mean diameter (D_m). Many empirical relations of the form $Z_m = aX^b$ ($X = R$, M, D_m, etc.), where a and b are coefficients, have been established for various latitudes, various seasons, and for different kinds of precipitation (stratiform or convective) and hydrometeors (rain, snow, hail) (e.g., Atlas 1990; Sauvageot 1992; Doviak and Zrnić 1993).

Electromagnetic wave propagation through the atmosphere can, however, be highly perturbed by clouds and precipitation, due to absorption and scattering. Radar retrieval of cloud and precipitation physical properties is thus limited by attenuation phenomena. Attenuation is defined (Glickman 2000) as a general term in which scattering and absorption are included. Herein, for the sake of simplicity, and because radar frequencies are in a domain where the attenuation of atmospheric gases is low, only attenuation by hydro-

Corresponding author address: Olivier Pujol, Laboratoire d'Aérologie, Observatoire Midi-Pyrénées, Université Paul Sabatier, 14 Ave. Édouard Belin, Toulouse 31400, France.
E-mail: pujo@aero.obs-mip.fr

DOI: 10.1175/JTECH1992.1

meteors is considered. The radar reflectivity factor Z_m (in dBZ) measured at a distance r (km) along the radar beam, can thus be written

$$Z_m(r) = Z(r) - \int_0^r a(r)\, dr, \quad (1)$$

where $Z(r)$ is the "true" radar reflectivity factor (in dBZ), that is, the radar reflectivity factor that would be observed without any attenuation, and $a(r)$ is the two-way attenuation coefficient (in dB km^{-1}) due to hydrometeors. Coefficient $a(r)$ depends mainly on the radar wave frequency (f): the higher the frequency, the stronger the attenuation (Stratton 1941). Consequently, for a given f, Z_m must be corrected from attenuation if reliable information on cloud and precipitation physics has to be deduced.

Several methods have thus been developed to retrieve from radar observations attenuation fields due to precipitation. The stereo-radar, or dual-beam radar method, is based on stereoscopic observations, that is, on two non-co-linear radar observations conducted at the same frequency. The corresponding attenuation field is then retrieved from a mathematical algorithm and used to correct the radar reflectivity values. This method was first proposed by Srivastava and Jameson (1977). It was applied by Testud and Amayenc (1989) for airborne radars observing rain cells and by Srivastava and Tian (1996) for ground-based radars. Applications to real cases were performed during the Tropical Ocean Global Atmosphere Coupled Ocean–Atmosphere Research Experiment (TOGA COARE) (Oury et al. 1998) for rainfall estimations from X-band airborne radar reflectivities. For airborne or space-borne observations, another usable method is the surface reference technique (SRT). It consists of comparing the reflectivity of a reference target (ocean or ground) with and without precipitation (Meneghini and Kozu 1990; Meneghini et al. 2000). The difference between the two radar measurements is then attributed to attenuation between the surface and the radar. Through simulations of space-borne radar observations of intense convective systems, Yeh et al. (1995) investigate the attenuation by precipitation and propose a rain-rate retrieval algorithm. Multifrequency radars are also a way of determining attenuation. In the dual-frequency mode, the same observation is conducted at two different frequencies: one weakly attenuated and the other more strongly so. Attenuation is then retrieved from the reflectivity differences. This technique was proposed by Eccles and Mueller (1971) in order to link the attenuation and the rainwater content. Gosset and Sauvageot (1992) used this approach in mixed-phase clouds to discriminate supercooled water and ice, and to estimate the mass content in each phase. The dual-frequency method was also used for hail detection (Atlas and Ludlam 1961; Eccles and Atlas 1973; Féral et al. 2003), rainfall estimation (Goldhirsh and Katz 1974), characterization of liquid and ice particles (Vivekanandan et al. 1999), or crystal sizing in cirrus (Hogan et al. 2000). To identify the non-Rayleigh effects due to the presence of large hydrometeors that affect the two-wavelength algorithm, Gaussiat et al. (2003) proposed a three-wavelength algorithm.

The nonprecipitating part of condensed atmospheric water (cloud component) can significantly affect electromagnetic wave propagation. Yet only attenuation by precipitation is generally taken into account in the correction of the observed reflectivity fields. Some orders of magnitude of cloud attenuation can be found in the literature. For example, for an observation at 50 km from the radar through a cloud at 0°C with a liquid water content of 1 g m^{-3}, attenuation is about 9 dB at the commonly used frequency $f = 10$ GHz (Sauvageot 1992); at $f = 94$ GHz, the same two-way attenuation is obtained through a path of only 1 km within the same cloud (Meneghini and Kozu 1990). As a consequence, the minimum detectable radar reflectivity increases by about 9 dB over a 50-km distance at 10 GHz and 1 km at 94 GHz. Lhermitte (1990) emphasized that strong cloud attenuation may seriously reduce the sensitivity of high-frequency radars ($f \geq 10$ GHz), in particular airborne and space-borne radars that typically operate at these frequencies to minimize their payload size. Cloud attenuation is obviously not negligible and has to be considered to avoid biased reflectivity fields, especially when observations are conducted with frequencies equal or greater than 10 GHz.

Unfortunately, clouds are frequently undetectable in reflectivity fields because their reflectivity is lower than the radar sensitivity threshold. According to Gossard and Strauch (1983), Sauvageot and Omar (1987), and Meneghini and Kozu (1990), typical nonprecipitating liquid cloud reflectivity values range from −50 to −20 dBZ for stratocumulus, from −45 to −17 dBZ for nimbostratus, and from −37 to 0 dBZ for cumulus. The problem of clouds is also evocated in Doviak and Zrnić (1993) where some orders of magnitude on cloud reflectivity and attenuation are given.

The goal and originality of this paper is to quantify by means of simulated radar observations at various frequencies the effects of cloud attenuation on the retrieved reflectivity fields. All the simulated observations concern warm precipitating cells: clouds are composed of liquid water droplets, and precipitation is only rain or drizzle. The ice phase is disregarded. Two kinds

of meteorological targets are first studied: a convective cell consisting of an isolated cumulus congestus associated with rain and, then, a stratiform cloud with drizzle superimposed on the previous convective cell. Other types of cumulus with different microphysical and geometrical cumulus characteristics are also considered. According to Glickman (2000), it is reasonable to represent warm clouds by cumulus clouds composed of a great number of small droplets; the nimbostratus background can also be considered as being composed of only liquid water droplets.

Section 2 concerns details relative to the modeling of meteorological targets and the simulation of radar observations. The microphysical and geometrical characteristics of the modeled cloud and precipitation fields are described and general considerations about attenuation by cloud droplets are given. Characteristics of the radar beam modeling and the configuration of the simulated observations are presented. Section 3 presents the results of the simulations for the two first targets considered. A further development is then made in section 4: considering different kinds of cumulus with various sizes, quantitative information about cumulus attenuation is given. In particular, attenuation is related to cumulus microphysics. Finally, conclusions and perspectives follow in section 5.

2. Modeling

a. Meteorological targets

The meteorological targets are made exclusively of liquid water with two distinct and independent parts: cloud and precipitation. In the model, cloud and rain/drizzle components are superimposed and do not interact, which means that the physical characteristics of one part can be modified without influencing the other one. Moreover, it becomes possible to superimpose independently several different components and to construct meteorological targets of diverse complexity. The simplest target considered, which is used to exemplify the simulation, is a convective cell consisting of a cumulus congestus associated with rain reaching the ground.

Cloud and rain fields are both represented by their respective liquid water content M_α ($\alpha = c$ for cloud and r for rain), supposed to be a spatial two-dimensional function, $M_\alpha(x, z) = G_\alpha(x)M_\alpha(z)$, where z is the vertical coordinate and G_α a weighting function depending on the horizontal coordinate x; for a given altitude z, the modulation of $M_\alpha(z)$ by $G_\alpha(x)$ determines $M_\alpha(x)$. Consequently, given $G_\alpha(x)$ and, independently, $M_\alpha(z)$, the α-fields geometry along x and z is defined.

Numerous observations on cumulus clouds (Zaitsev 1950; Warner 1955, 1969, 1970; Squires 1958; Borovikov 1963; Mason 1971; Vulfson et al. 1973; and others) have shown that M_c is closely related to the global cloud dynamic structure. Typically, $M_c(z)$ increases with height above cloud base, reaches a maximum value $M_c^{\max}$ in the upper half of the cloud, and then decreases up to cloud top. In the present model, cloud base is at an altitude of 1 km, cloud thickness e is 2 km, and $M_c^{\max} \approx 3$ g m^{-3} at about 600 m under cloud top (Fig. 1a). Moreover, at cloud base and cloud top, $M_c(z)$ is equal to a limit value of 0.2 g m^{-3}, to represent the well-marked transition between the cloud and its clear-air environment. The value of $M_c(x)$ globally decreases from cloud center to cloud periphery. It is modeled by considering $G_c(x)$ as a function of the following form: $G_c(x) = \exp(-x^2/\mathrm{SD}^2)$ with SD = 5 km. Here, SD is supposed to conventionally define the horizontal cloud extension L, so that $L = 2 \times \mathrm{SD} = 10$ km (Fig. 1b). The cloud shape factor is then $s_f = L/e = 5$. Thus, multiplying $M_c(z)$ by $G_c(x)$ gives the cloud water content M_c; its maximum is about 3 g m^{-3} at an altitude of 2.5 km along the cloud axis. According to Borovikov (1963), who considers that cloud water content of cumulus congestus ranges from 0.5 to 3 g m^{-3}, this cumulus can be described as a dense and vigorous one, so that it will be hereafter qualified as "extreme." Cloud geometry is defined by imposing, in the model, $M_c \geq 0.2$ g m^{-3}, while all the others values are put to zero. Horizontal edges of the cloud are also determined in the same way.

For vertical rainwater content, Blanchard (1953) and Okita (1958) pointed out that a maximum value $M_r^{\max}$ is generally located just below cloud base. Figure 2 represents the variation of $M_r(z)$ with altitude z. Because of evaporation, $M_r(z)$ decreases from $M_r^{\max} = 0.46$ g m^{-3} at $z = 0.9$ km to a value of about 0.1 g m^{-3} at the ground ($z = 0$). Obviously, M_r decreases upward in cloud and is zero at cloud top. Along x, rainwater content tends to be maximum straight below the cloud axis and minimum at cloud edges because of air circulations consisting of updrafts near the cloud axis and downdrafts at the cloud edges. The modulating function $G_r(x)$ is therefore the same as $G_c(x)$ (Fig. 1b). Thus, multiplying $M_r(z)$ by $G_r(x)$ gives the rainwater content M_r; its maximum is about 0.46 g m^{-3} at the altitude of 0.9 km along the cloud axis. In the model, M_r values lower than 0.04 g m^{-3} are equaled to zero in order to define the rain-space domain.

Superimposition of $M_c(x, z)$ and $M_r(x, z)$ leads to the modeling of the meteorological target. The values of all the parameters used to model the cloud are issued from the studies mentioned in this section and on numerous observations. It is then assumed that they are representative of realistic field values.

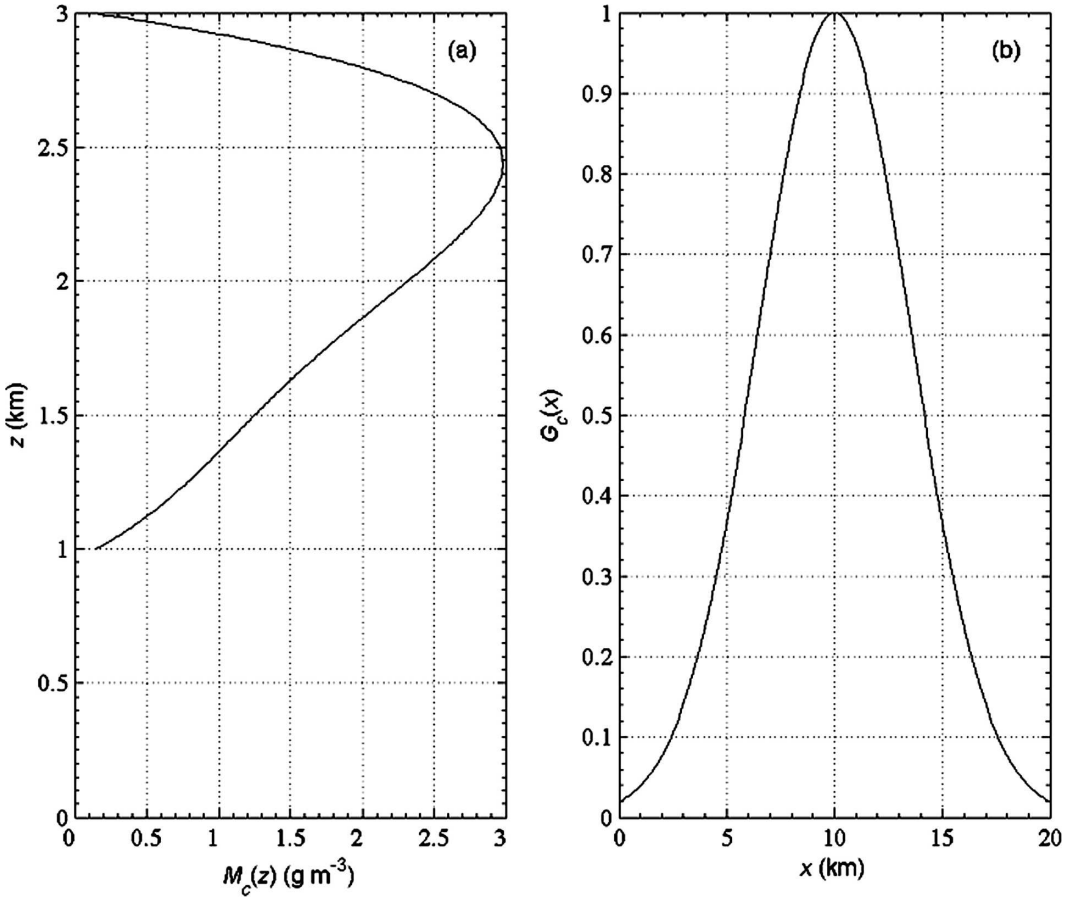

FIG. 1. (a) Vertical dependence of cloud liquid water content $M_c(z)$; cloud base and cloud top are, respectively, at the altitudes of 1 and 3 km. At these altitudes, cloud water content is set approximately to 0.2 g m^{-3} in order to create a transition between the cloud and its clear-air environment. (b) Weighting function $G_c(x)$ modulating $M_c(z)$ at a given altitude z to define the cloud liquid water content horizontal dependence $M_c(x)$.

b. Scatterer size distribution

A complete microphysical target modeling requires specifying the size distributions of the hydrometeors, that is, cloud droplets and raindrops.

It is reasonable and convenient to represent the cloud droplet size distribution (CDSD) by a gamma distribution, for example, the Khrgian and Mazin (1952) distribution:

$$N_c(D_c) = N_0 D_c^2 \exp(-\Lambda D_c), \tag{2}$$

where D_c is the cloud droplet diameter, N_c the volumic concentration per class of diameter (i.e., the number of droplets with diameters between D_c and $D_c + \Delta D_c$ per unit volume), and N_0 and Λ are parameters that can be related to any two moments of the distribution, as the total droplet concentration N_t (zeroth-order moment) and liquid water content M_c (proportional to the third-order moment). If the water density ρ_w is (g cm^{-3}), D_c is expressed in centimeters, N_t (cm^{-3}) and M_c (g m^{-3}), the Khrgian and Mazin (1952) distribution gives $N_c(D_c)$ (cm^{-3} μm^{-1}), with

$$N_0(\text{cm}^{-6}) \approx 1.27 \times 10^4 \left(\frac{\rho_w N_t^2}{M_c}\right)$$

and

$$\Lambda(\text{cm}^{-1}) \approx 3.16 \times 10^2 \left(\frac{\rho_w N_t}{M_c}\right)^{1/3}.$$

In the present work, a droplet size interval ΔD_c of 1 μm and a maximum droplet diameter of 50 μm are considered so that 50 diameter classes, centered on the successive diameter values $(D_{c,\,i})_{i=1\ldots50} = \{0.5, 0.15, \ldots, 48.5, 49.5\ \mu\text{m}\}$, are defined. The knowledge of M_c and N_t thus enables the determination of the CDSD. It is assumed that N_t is constant and equal to 350 cm^{-3} throughout the cumulus (Borovikov 1963; Pruppacher

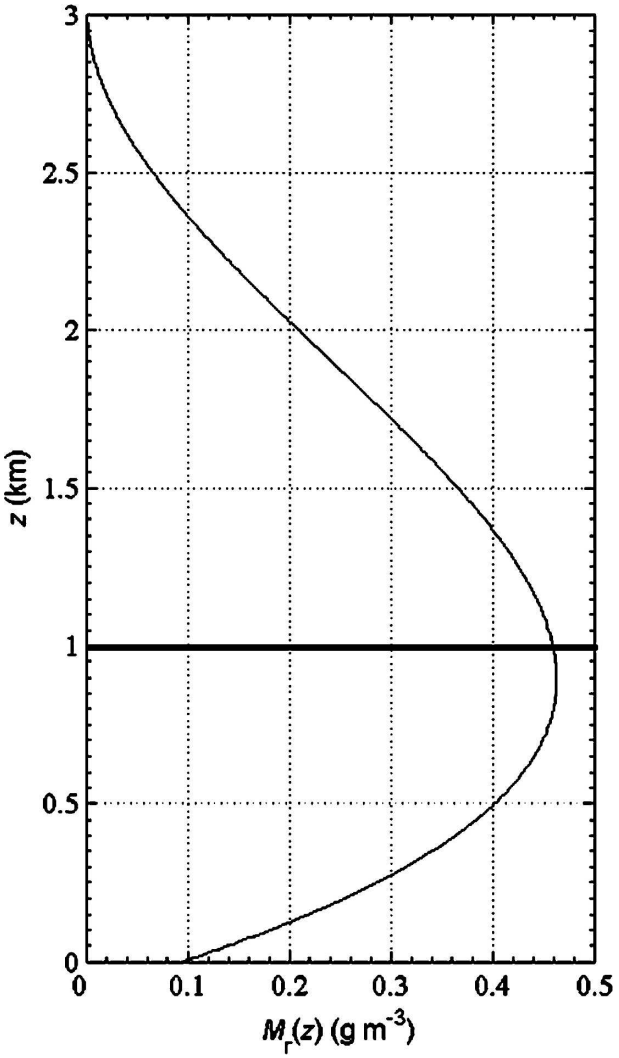

FIG. 2. Rainwater content vertical dependence $M_r(z)$; the solid line at $z = 1$ km represents the cloud base. Cloud top is at $z = 3$ km.

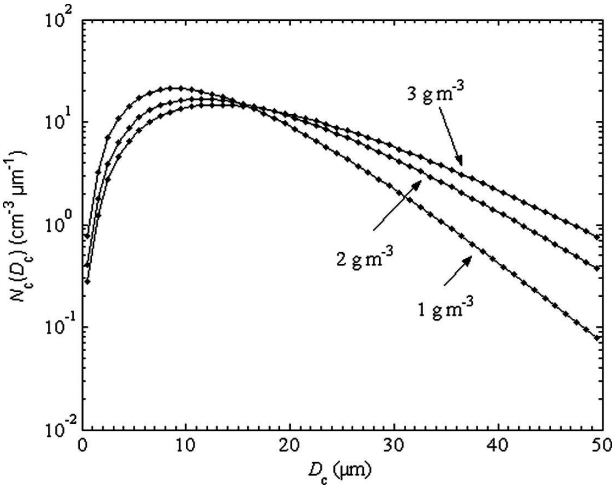

FIG. 3. CDSD represented by a Khrgian and Mazin (1952) distribution. CDSD is displayed for three values of the cloud liquid water content and for a total droplet concentration fixed at 350 cm^{-3}. Here, D_c is the droplet diameter and N_c the volumic concentration per diameter class.

and Klett 1997, section 2.1). Figure 3 displays the CDSD for different values of M_c and shows concentrations ranging from 0.08 to 20 cm^{-3} μm^{-1}, which is consistent with the different orders of magnitude summarized in Pruppacher and Klett (1997, section 2.1).

According to Ulbrich (1983), raindrop size distribution can be represented by a two-parameter modified gamma distribution of the form

$$N_r(D_r) = N_0 D_r^{\mu} \exp(-\Lambda D_r), \tag{3}$$

where D_r is the drop diameter, N_r the volumic concentration per class of diameter (i.e., the number of raindrops with diameters between D_r and $D_r + \Delta D_r$ per unit volume), and N_0, μ, and Λ are parameters. Moreover, Λ (mm^{-1}) is related to the median diameter D_0(mm) by the relationship $\Lambda D_0 = 3.67 + \mu$. If D_r (mm) and M_r (g m^{-3}), then

$$N_0\,(\mathrm{m}^{-3}\,\mathrm{mm}^{-1-\mu}) = \left[\frac{6}{\pi\Gamma(\mu+4)}\right]\left(\frac{M_r}{10^{-3}\rho_w}\right) \times \left(\frac{3.67+\mu}{D_0}\right)^{\mu+4},$$

where Γ is the gamma function, so that $N_r(D_r)$ (m^{-3} mm^{-1}). In the present study, a drop size interval ΔD_r of 0.1 mm and a maximum drop diameter of 5 mm are considered so that 50 diameter classes, centered on the successive diameter values $(D_{r,\,i})_{i=1\ldots50} = \{0.05, 0.15, \ldots, 4.85, 4.95$ mm$\}$, are defined. The knowledge of M_r, D_0, and μ thus enables the determination of the raindrop size distribution (RDSD). It is assumed that D_0 is constant and equal to 2 mm throughout the rain field, a value frequently encountered in the bibliography (e.g., Ulbrich 1983, Fig. 2). A particular point of the RDSD concerns the smallest raindrops, which evaporate rapidly outside the cloud because the atmosphere is drier than it is inside. This implies that their concentration falls down significantly within a relatively very short distance from of the cloud. The smaller the raindrop, the faster it evaporates, and the lower the concentration is. Ulbrich (1983) indicates that various physical processes in unsaturated air, such as evaporation, seem to transform an RDSD defined by $\mu = 0$ inside a cloud to a gamma distribution with $\mu > 0$ outside a cloud. Therefore, in the simulation, it is reasonable to take μ

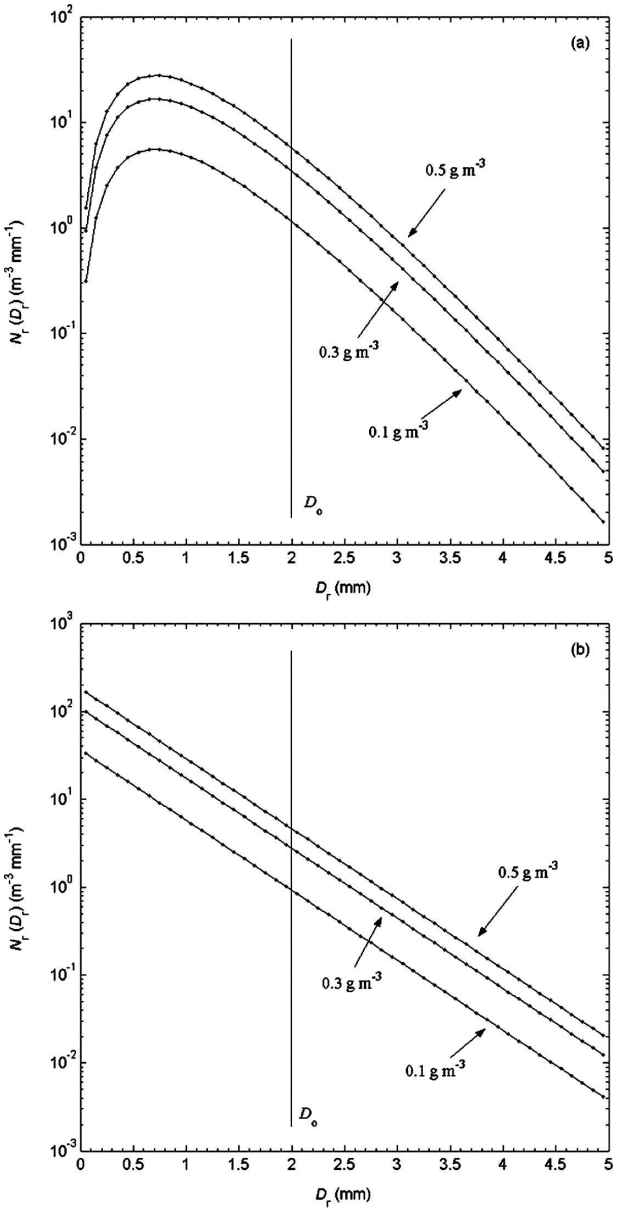

FIG. 4. RDSD represented by a gamma distribution. RDSD is displayed for three values of the rainwater content and for a median diameter D_0 fixed at 2 mm (represented by the black vertical line). Here, D_r is the raindrop diameter and N_r the volumic concentration per diameter class. RDSD with (a) $\mu = 2$ and (b) $= 0$.

equal to zero inside the cloud and equal to 2 outside so that small raindrops are in greater concentration within the cloud. In that sense, smaller drops can represent drizzle drops defined as drops of diameters smaller than 0.5 mm (Glickman 2000). Figure 4 shows the RDSD for different values of M_r for $\mu = 0$ (Fig. 4a) and $\mu = 2$ (Fig. 4b); concentration ranges from 10^{-3} to 10^{2} m^{-3} mm^{-1}.

c. Backscattering and attenuation cross sections

Backscattering (σ) and attenuation (Q) cross sections of a spherical scatterer are given by the Mie formulas (Mie 1908), whose coefficients are computed with the Deirmendjian (1969) algorithm. These coefficients depend on the radar frequency (f), on the spherical diameter, and on the complex index of the refraction $m = n + i\kappa$ of the scatterer. The latter is computed using the Ray (1972) model, assuming that cloud and rainwater temperatures are 5°C. Thus, σ and Q are computed for all the hydrometeors under consideration in the simulation, that is $(\sigma_i)_{i=1...50}$ and $(Q_i)_{i=1...50}$ for the homogeneous spherical particles of diameter $(D_i)_{i=1...50}$ constituting the cloud and the rain field.

For cloud droplets, D_c is small enough with respect to the radar wavelength ($\lambda = c/f$) to satisfy the conditions of the Rayleigh approximation. In addition, for such particles, scattering is small with respect to absorption and, consequently, attenuation cross-section Q can be considered equal to the absorption cross-section Q_a. In this context, the two-way cloud attenuation a_c(dB km^{-1}) is independent from the size spectrum and proportional to the liquid water content M_c:

$$a_c = 2 \times 0.4343 \int_{D_{c,\min}}^{D_{c,\max}} N_c(D_c) Q_a(D_c)\, dD_c = kM_c, \tag{4}$$

where Q (cm^3), the other parameters are as in (2), and k depends on λ and on the temperature. Figure 5 displays the coefficient k for cloud droplets as a function of λ ranging from 0.1 to 10 cm, for a temperature of 5°C. It clearly shows that cloud attenuation is a nonnegligible effect that must be taken into account in radar measurements. For example, at 94 GHz ($\lambda = 3.2$ mm), the two-way cloud attenuation at 0°C is about 10 dB for a 1-km path; at 10 GHz ($\lambda = 3.2$ cm), under the same conditions, the two-way attenuation is only 0.2 dB, but it can be a nonnegligible quantity for longer paths. Liquid water attenuation is not very sensitive to temperature, and much more attenuating than ice (e.g., Sauvageot 1992, Fig. 2.14, p. 105). Also, in a first approach, the ice phase is intentionally omitted and the cloud temperature is uniform.

d. Equivalent radar reflectivity factor

The average power backscattered by a population of particles homogeneously distributed in an elementary volume V is proportional to the radar reflectivity η, defined as the sum of the backscattering cross sections (σ_i) of the individual particles:

$$\eta = \frac{1}{V}\sum_i \sigma_i, \tag{5}$$

where η is commonly expressed in per centimeter. When the observed scattering volume does not satisfy the conditions of the Rayleigh approximation, or if there is any doubt that it does, it is convenient to characterize the radar reflectivity factor Z by the equivalent radar reflectivity factor Z_e, which is, by definition, equal to the radar reflectivity factor of a population of liquid and spherical particles satisfying the Rayleigh approximation and producing a signal of the same power (e.g., Atlas 1990):

$$Z_e\,(\mathrm{mm^6 m^{-3}}) = \frac{\eta}{2.8 \times 10^{-10}\lambda^{-4}}, \tag{6}$$

where λ is in centimeters. Usually, Z_e is expressed in a logarithmic unit:

$$Z_e\,(\mathrm{dBZ}) = 10\log[Z_e\,(\mathrm{mm^6 m^{-3}})]. \tag{7}$$

e. Radar beam modeling and meshing

Nowadays, radars operate with various frequencies corresponding to wavelengths ranging from the millimetric to the centimetric domain of the electromagnetic spectrum. For example, S (f = 3 GHz, $\lambda \approx 10$ cm), X (f = 10 GHz, $\lambda \approx 3$ cm), K_a (f = 35 GHz, $\lambda \approx 0.86$ cm), or W (f = 94 GHz, $\lambda \approx 0.32$ cm) bands are common in radar observations, and the choice of f depends upon the application. Generally, in order to reduce the equipment size and weight, airborne and space-borne radars operate at frequencies close to or higher than 10 GHz. Other advantages of these kinds of radars are their relatively high resolution.

In the present work, radar observations are simulated for the four above-mentioned frequencies. The modeled radar beam is characterized by a cone of aperture approximated to the 3-dB beamwidth ($\theta_{3\mathrm{dB}}$) and the range gate spacing is Δr. The meteorological target is digitized through a two-dimensional meshing with grid resolutions of 100 and 10 m along the horizontal and vertical axes, respectively. Each grid point is characterized by specific values of M_c and M_r and, consequently, by specific CDSDs and RDSDs. The computational procedure consists, at first, of a given resolution volume V, in identifying the grid points included in V and characterized by M_c and/or M_r different from zero. For each of these grid points, the backscattering and attenuation cross sections of all the hydrometeors (i) are computed ($\sigma = \Sigma_i \sigma_i$ and $Q = \Sigma_i Q_i$, respectively). Then, η associated with V is deduced from (5) and, finally, Z_e (dBZ) is obtained from (6) and (7).

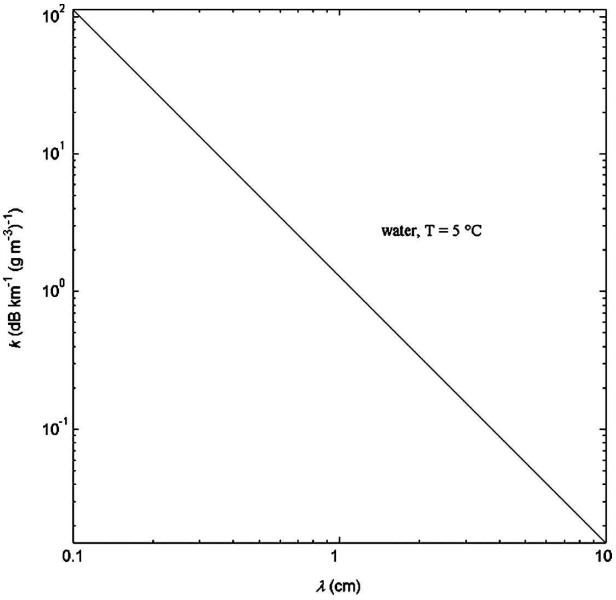

FIG. 5. Two-way cloud attenuation k as a function of the radar wavelength λ for a cloud liquid water content equal to 1 g m^{-3} and a droplet temperature of 5°C.

By the same procedure, only the cloud attenuation (which is within the scope of this paper) undergone by the radar beam during the crossing of the target is calculated using (4) for each V. Thus, the equivalent reflectivity factor Z_e, degraded by a_c, is

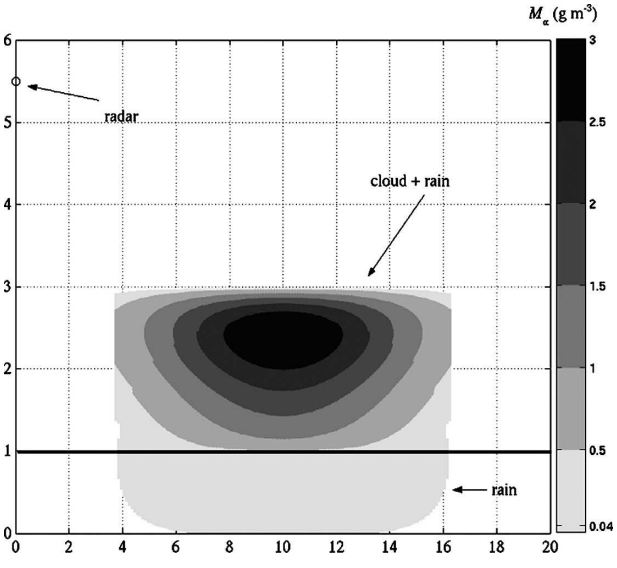

FIG. 6. Representation of the modeled convective cell in terms of liquid water content M_α. This cell consists of a cumulus cloud associated with a rain field reaching the ground. The black horizontal solid line represents the cloud base. Observations of this cell are performed with an airborne radar located at (x, z) = (0, 5.5 km) symbolized by "o."

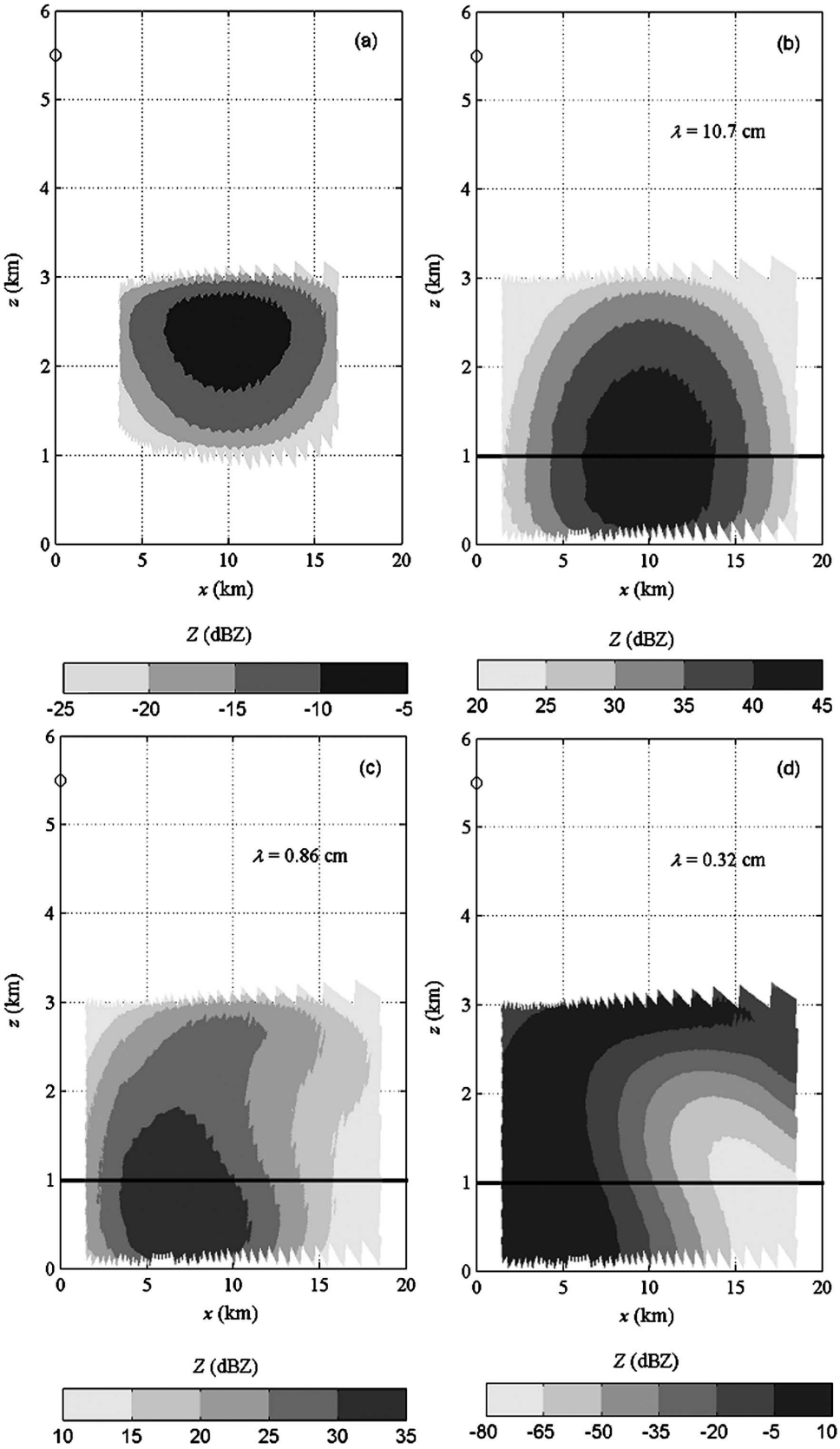

FIG. 7. Simulation of the observed reflectivity fields. (a) Cumulus cloud reflectivity at the reference wavelength 10.7 cm. (b)–(d) Reflectivity fields degraded by the cloud attenuation at 10.7, 0.86, and 0.32 cm, respectively. Radar is represented by the symbol "o" at $(x, z) = (0, 5.5$ km).

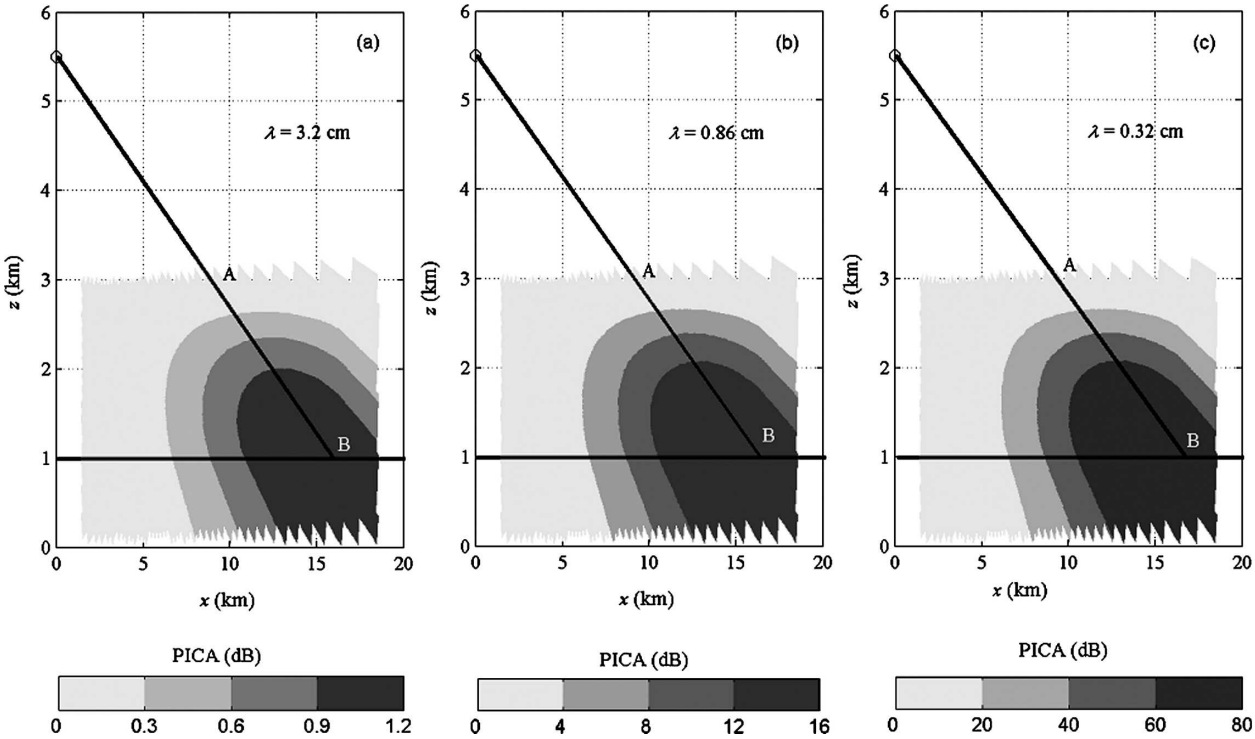

FIG. 8. PICA, relative to 10.7 cm, at (a) 3.2, (b) 0.86, and (c) 0.32 cm. The black horizontal solid line represents the cloud base while the diagonal one represents a radial issued from the radar (symbol "o" at $x = 0$ km and $z = 5.5$ km). Points A and B mark the distance propagated by the radar wave into the cloud; distance AB is about 5.4 km.

$$[Z_e\,(\mathrm{dB}Z)]_{\mathrm{degraded}} = Z_e\,(\mathrm{dBZ}) - \int_0^r a_c(r)\,dr. \quad (8)$$

The simulation is fully completed when the successive radar beams, separated by $\Delta\beta$ in the azimuth, have covered the whole extent of the target.

3. Results and discussion

The considered cumulus congestus and the associated rain field are displayed in Fig. 6. As already indicated in section 2, cloud liquid and rainwater contents have maximum values of about 3 and 0.5 g m^{-3}, respectively; the cloud thickness is $e = 2$ km; and the horizontal extension of the cell is $L = 10$ km, so that the shape factor is 5. It is noteworthy to recall that these values, derived from observations, correspond to a vigorous cumulus congestus (Borovikov 1963). So as to quantitatively assess the cloud attenuation endured by an airborne radar, the latter located above the cumulus at a mean altitude of 5.5 km, in compliance with real operational conditions. The radar is thus at $x = 0$ km in Fig. 6 and the following (symbol "o"). Four different wavelengths (10.7, 3.2, 0.86, and 0.32 cm) are considered in the simulation. Moreover, the radar has a common aperture $\theta_{3\mathrm{dB}}$ and a gate spacing Δr equal to 1.8° and 0.15 km, respectively. These values are frequently used in airborne radar. For instance, the Electra Doppler Radar (ELDORA) is characterized by an aperture of 1.8° and a gate spacing of 150 m. These characteristics have been kept whatever the wavelength because they are not crucial in the present work and do not affect the results since they only concern the volume of resolution. An azimuth spacing of $\Delta\beta$ is chosen at a common value of 1°.

a. Reflectivity and cloud attenuation fields derived from simulations

Simulated reflectivity fields are displayed in Fig. 7. Cumulus cloud reflectivity is shown in Fig. 7a. It can be noted that, because cloud particles are in the Rayleigh scattering region, the reflectivity of the cumulus does not depend on the wavelength so that Fig. 7a is valid whatever the wavelength considered in this paper. Reflectivity fields degraded by cloud attenuation $[Z_e\,(\mathrm{dB}Z)]_{\mathrm{degraded}}$ (8), hereafter denoted $Z_{e,d}$ ("d" for degraded), are displayed in Figs. 7b–d for three wavelengths: 10.7, 0.86, and 0.32 cm, respectively. At 10.7 (Fig. 7b) and 3.2 cm (not shown), the reflectivity fields are quite similar and representative of the precipitating cell with $Z_{e,d}$ ranging from low values (20 dBZ) at the

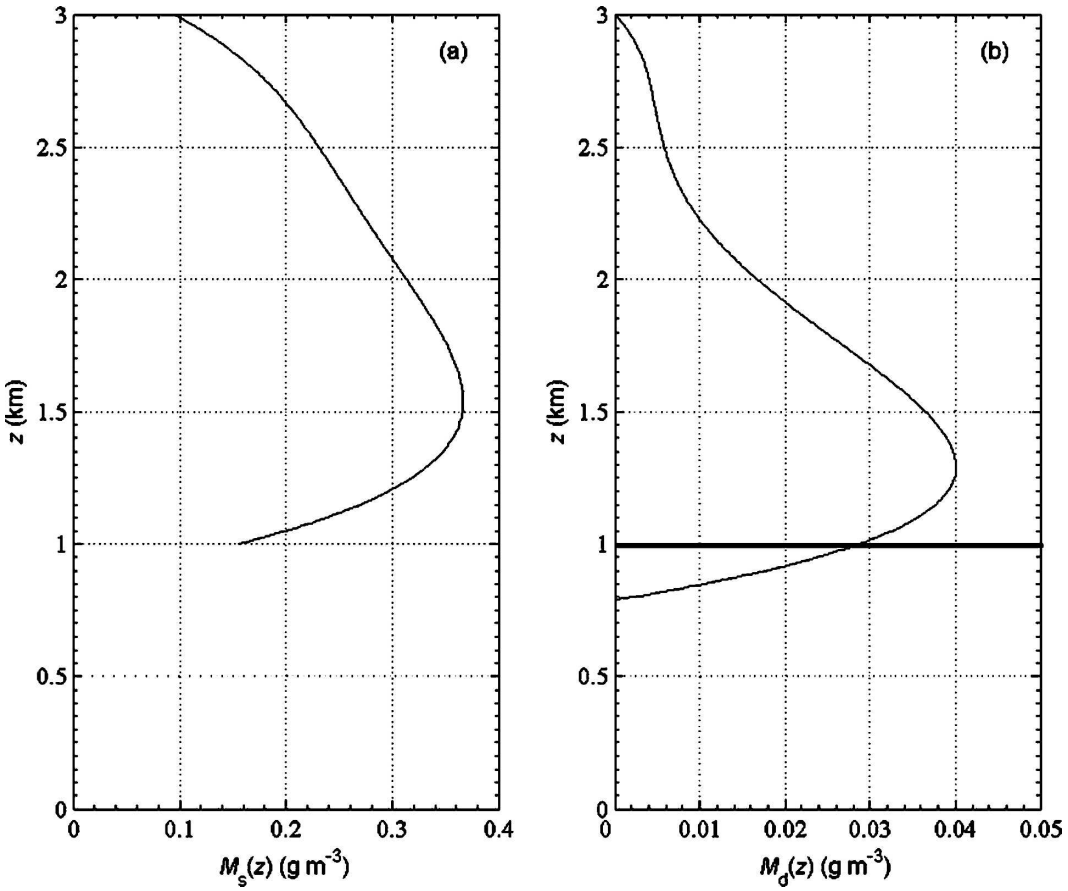

FIG. 9. (a) Vertical profile of stratiform cloud liquid water content $M_s(z)$; cloud base and cloud top are at altitudes of 1 and 3 km, respectively. At these altitudes, cloud water content is set to 0.1 g m^{-3} to separate the cloud and its clear-air environment. (b) Vertical profile of drizzle liquid water content $M_d(z)$; cloud base ($z = 1$ km) is represented by the black horizontal solid line and cloud top is at the altitude of 3 km. Drizzle does not reach the ground because of evaporation and $M_d(z)$ is equal to zero at an altitude of about 800 m.

edges of the cell to higher values (40 dBZ) in the core of the cell (0.2 km $< z <$ 2 km) where the rainwater content is maximum. At shorter wavelengths (0.86 and 0.32 cm), reflectivity fields are substantially different: $Z_{e,d}$ has lower values ranging from 10 to 35 dBZ at 0.86 cm (Fig. 7c) and from -80 to 10 dBZ at 0.32 cm (Fig. 7d). Moreover, reflectivity fields are highly distorted and clearly show the importance of the cloud attenuation, which is all the higher as the distance covered within the cloud is increased.

As shown in Fig. 5, the attenuation at 10.7 cm is negligible so that its reflectivity $Z_e^{10.7}$ can be considered to be a reference. Consequently, whatever the wavelength λ, (8) can be written as follows:

$$Z_e^{10.7} - Z_{e,d}^{\lambda} \approx \mathrm{A} + \mathrm{B}$$

$$\text{with} \quad \mathrm{A} = (Z_e^{10.7} - Z_e^{\lambda}) \quad \text{and} \quad \mathrm{B} = \int_0^r a_c^{\lambda}\, dr. \quad (9)$$

Figure 8 displays the term B, the two-way path-integrated cloud attenuation (PICA), for the three lowest wavelengths: 3.2 (Fig. 8a), 0.86 (Fig. 8b), and 0.32 cm (Fig. 8c). As expected, the shorter the wavelength, the higher the attenuation: maximum values are about 1.2 dB at 3.2 cm, 16 dB at 0.86 cm, and 80 dB at 0.32 cm. These areas of maximum attenuation are coincident with the regions where the reflectivity is the lowest (Fig. 7). This means that, in these regions, the reflectivity fields are the most degraded. These highest attenuation values are consistent with the orders of magnitude provided in Fig. 5: considering a cloud with a unit water content (g m^{-3}), the attenuation is about 0.18 dB at 3.2 cm, 2.4 dB at 0.86 cm, and 12 dB at 0.32 cm for a radar wave propagating over 1 km into the cloud. Therefore, as the distance propagated into the cloud between the cloud top and the region of maximum attenuation (distance AB in Fig. 8) is approximately AB $= e(1 + s_f^2/4)^{1/2} = 5.4$ km for the considered cell, the values de-

rived from the simulation correspond to a cloud water content around 1.2 g m^{-3}, which is consistent with the characteristics of the considered cloud (section 2). This gives credit to the simple model used to represent the meteorological targets and their microphysical content, and to simulate radar observations. In addition, it clearly appears that clouds can induce a strong attenuation on radar wave although they have a low reflectivity, as shown in Fig. 7a relative to a simulated observation at the reference wavelength (10.7 cm). This is all the more problematic for radar observations because clouds are often undetectable due to their very low reflectivity values (between −25 and −5 dBZ for the considered cell). As a comparison, during TOGA COARE, the minimum detectable signal of the ELDORA/Analyze Stéréoscopique par Radar Aéroporté sur Electra (ASTRAIA) was −12 dBZ at 10 km (Hildebrand et al. 1994), the wavelength used by ELDORA being 3.2 cm (frequency of 9.6 GHz). For the 13.8-GHz Airborne Rain Mapping Radar (ARMAR), the theoretical minimum detectable reflectivity is about 10 dBZ at 10 km (Durden et al. 1994). This radar was designed as a prototype for the 13.8-GHz spaceborne rain radar on the Tropical Rainfall Measuring Mission (TRMM) satellite, which has a minimum detectable signal of 17 dBZ (e.g., Schumacher and Houze 2000). Cumulus clouds are thus partially, if not totally, undetectable (also see section 4 for other cumulus reflectivity values).

b. Influence of a stratiform background

A stratiform cloud associated with a drizzle field has been superimposed on the previous convective cell in order to quantify the effects of a stratiform background on the radar retrieval. As for the convective cell, the physical characteristics of the stratiform cloud are based on observations reported in the literature (e.g., Borovikov 1963; Pruppacher and Klett 1997, section 2.1). Figure 9 represents the vertical profile of the stratiform cloud water content, M_s (Fig. 9a), and of the drizzle water content, M_d (Fig. 9b). Here, M_s increases rapidly from 0.15 g m^{-3} at cloud base (z = 1 km) to a maximum value of about 0.35 g m^{-3} at z = 1.5 km. Above this altitude, M_s decreases upward gently to reach 0.1 g m^{-3} at cloud top (z = 3 km). On the other hand, M_d increases from zero at cloud top to reach a maximum value of 0.04 g m^{-3} at z = 1.3 km. Below cloud base, drizzle evaporates rapidly so that M_d is zero at z = 800 m. Along x (not shown), the modulating function $G(x)$ is uniform and equal to unity for both stratiform cloud and drizzle. The microphysical characteristics of the stratiform cloud are the same as those of the cumulus, except that

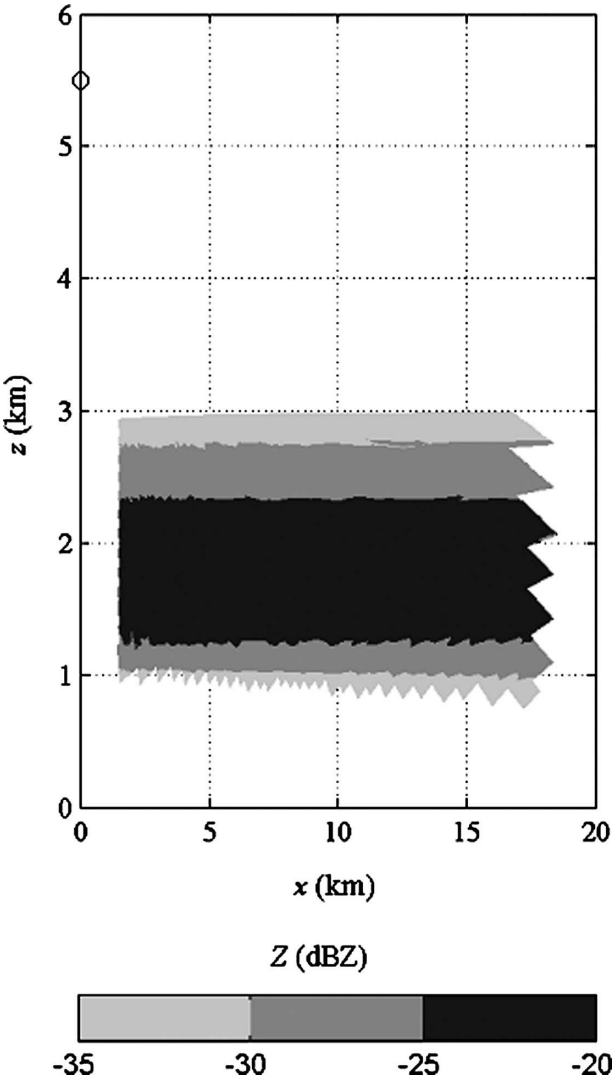

FIG. 10. Simulation of the observed stratiform cloud reflectivity at the reference wavelength of 10.7 cm. The radar is represented by symbol "o" at (x, z) = (0, 5.5 km).

- the maximum cloud droplet diameter is 30 μm and
- the minimum and maximum drizzle drop diameters are, respectively, 0.2 and 0.5 mm, according to the drizzle definition (Glickman 2000). The median drizzle drop diameter is 0.3 mm.

Using the same distribution as for the convective cell, cloud droplet and drizzle drop concentrations range, respectively, from 10^{-4} to 10^{2} cm^{-3} μm^{-1} and from 1 to 10^{2} m^{-3} mm^{-1} (distributions not shown). According to observations summarized in Borovikov (1963), these microphysical characteristics correspond to those of a nimbostratus cloud. Thus, the simulations are conducted with the same radars as in section 3, but they now concern a convective cell embedded in a stratiform

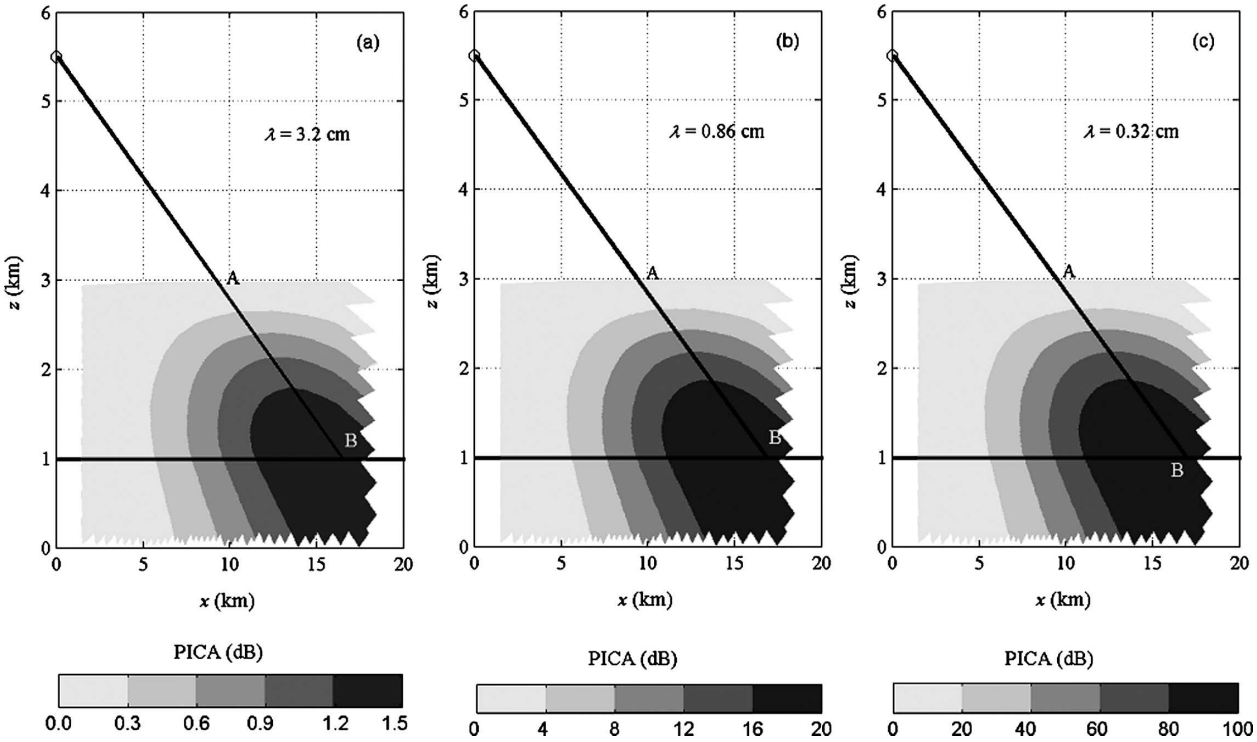

FIG. 11. PICA of the overall cloud component (cumulus plus nimbostratus), with respect to 10.7 cm, at (a) 3.2, (b) 0.86, and (c) 0.32 cm. The black horizontal solid line represents the cloud base while the diagonal represents a radial issued from the radar (symbol "o"). The points A and B mark the limits of the path propagated into the cloud; distance AB is about 5.4 km.

background consisting of a nimbostratus cloud with a drizzle field. Reflectivity is degraded by the attenuation caused by the cumulus and nimbostratus.

Figure 10 displays the stratiform (nimbostratus) cloud reflectivity, which is independent on the wavelength for the same reason as for the cumulus cloud. Values are lower than for the cumulus cloud and range from −35 to −20 dBZ. Degraded reflectivity fields (not shown) present the same characteristics as for the convective cell (section 3a) except that values are lower for the shortest wavelengths: they range from 0 to 30 dBZ at 0.86 cm and from −100 to 0 dBZ at 0.32 cm. At 10.7 and 3.2 cm, reflectivity values are quite similar because of the low attenuation at these wavelengths. It follows that attenuation by the overall cloud component (cumulus plus nimbostratus) is higher than above. Figures 11a–c display the total path-integrated cloud attenuation (PICA) at 3.2, 0.86, and 0.32 cm obtained in the same way as in section 3b. These figures indicate that PICA maximum values are about 1.5 dB (3.2 cm), 20 dB (0.86 cm), and 100 dB (0.32 cm), whereas they were about 1.2 dB (3.2 cm), 16 dB (0.86 cm), and 80 dB (0.32 cm) for cumulus only (Fig. 8). Hence, according to Fig. 5, the cumulus plus nimbostratus attenuation contribution is that of a cloud with uniform water content equal to about 1.5 g m^{-3}. Therefore, the contribution of the nimbostratus is 0.3 g m^{-3}. This value is consistent with the definition of the stratiform cloud in terms of water content adopted in this section. Thus, although strati-

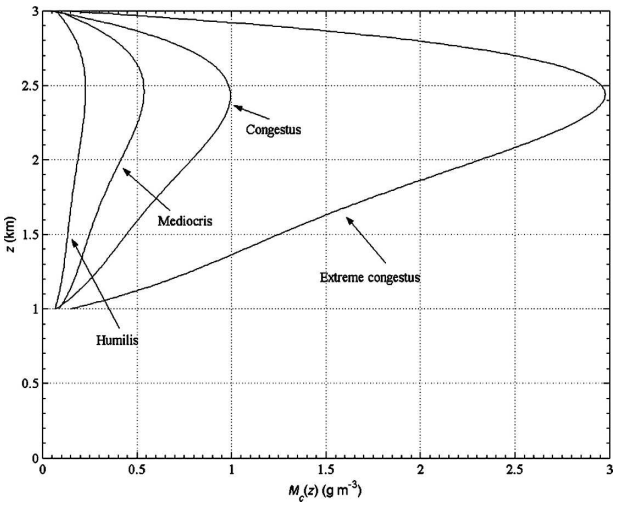

FIG. 12. Vertical profile $M_c(z)$ of the liquid water content for the various cumulus clouds considered. All of them have a thickness of 2 km and a shape factor of 5.

TABLE 1. PICA maximum values and cloud reflectivity ranges derived from simulations as a function of $M_c^{\max}$ and of the wavelength λ. Cumulus thickness and shape factor are, respectively, 2 km and 5.

$M_c^{\max}$ (g m^{-3})		3	1	0.5	0.2
PICA maximum values (dB): e = 2 km and s_f = 5	λ = 3.2 cm	1.2	0.5	0.3	0.10
	λ = 0.86 cm	16	7.0	4	1.5
	λ = 0.32 cm	80	35	20	7
Cloud reflectivity at 10.7 cm (dBZ)		−25 to −5	−35 to −15	−40 to −20	−45 to −25

form clouds have low reflectivities, their attenuation is not negligible.

c. Consequences

What ensues from the above-simulated observations is that the retrieval of precipitation physical properties from radar measurements can be seriously biased by cloud attenuation.

Indeed, according to Lhermitte (1990), a 1-dBZ uncertainty in radar reflectivity η measurements at millimeter wavelengths produces a mean uncertainty in rainfall precipitation R of 15% at 0.86 cm and 30% at 0.32 cm. Additionally, if quantitative information on cloud and precipitation microstructure has to be obtained from radar reflectivity, cloud attenuation has to be taken into consideration, especially at short wavelengths (Figs. 8b and 8c).

At centimeter wavelength (3.2 cm), although attenuation is lower than at millimeter wavelength, relative errors in physical quantities can be nonnegligible. For example, considering the power relation Z (mm^6 m^{-3}) = $300R$ (mm h^{-1})$^{1.35}$ proposed by Sekhon and Srivastava (1971) for convective rain associated with a thunderstorm or a cumulus congestus, $(R_{10})^{-1}\Delta R \approx 0.74(Z_{10})^{-1}\Delta Z$, where Z_{10} and R_{10} are the reference values at 10.7 cm and ΔZ is the difference

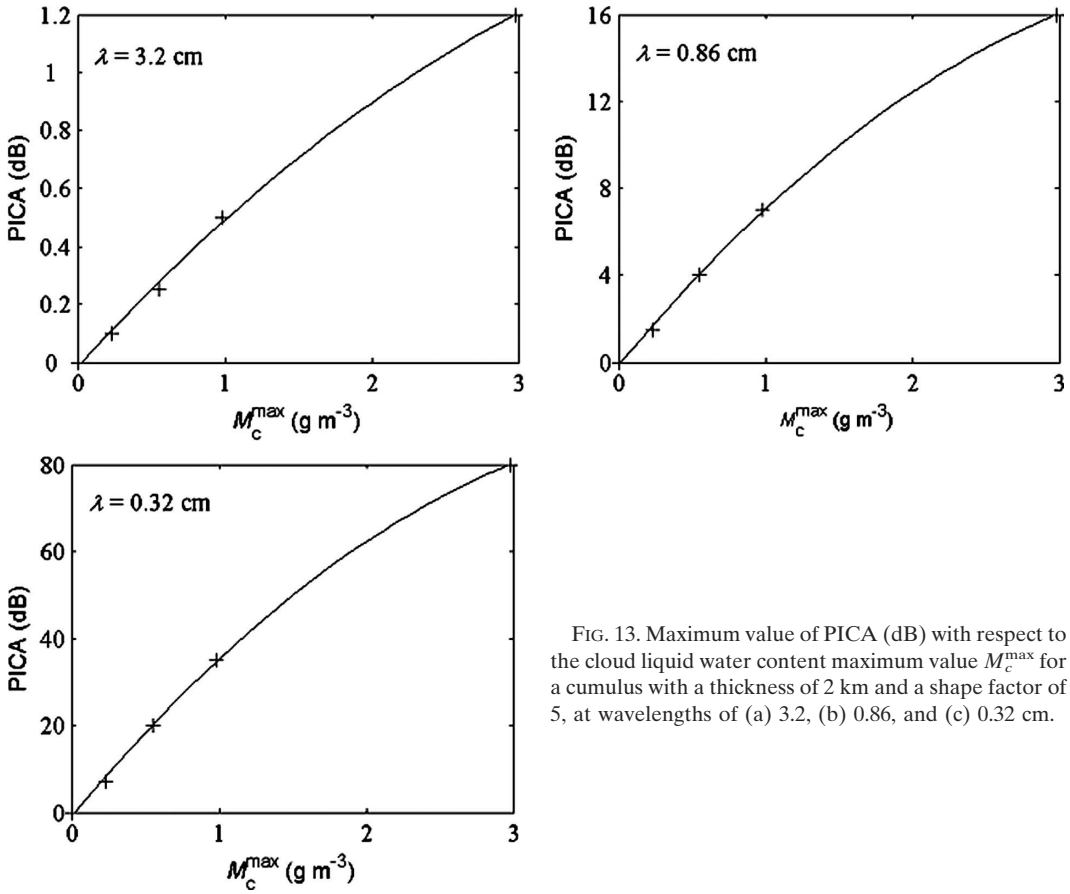

FIG. 13. Maximum value of PICA (dB) with respect to the cloud liquid water content maximum value $M_c^{\max}$ for a cumulus with a thickness of 2 km and a shape factor of 5, at wavelengths of (a) 3.2, (b) 0.86, and (c) 0.32 cm.

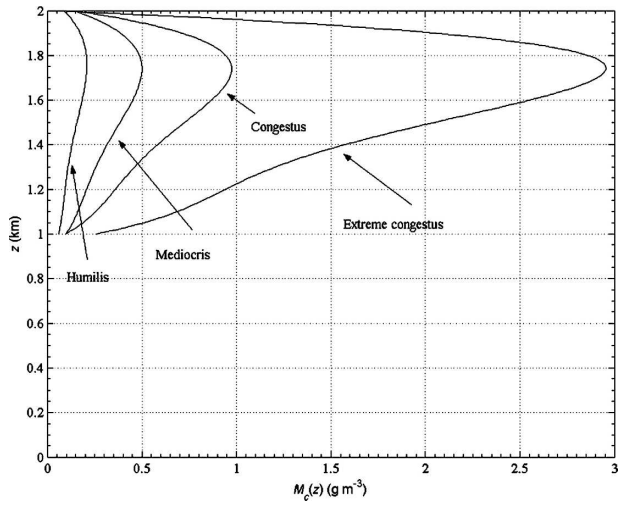

FIG. 14. Vertical profile $M_c(z)$ of the liquid water content for the various cumulus clouds considered. All of them have a thickness of 1 km and a shape factor of 5.

between the real degraded reflectivity and that of the cloud. This relation, valid only if the Rayleigh condition is satisfied, can obviously be applied to the present case concerning a cumulus congestus insofar as the drop diameter ranges from 0.1 to 5 mm (section 2). Considering that ΔZ is equal to the maximum cloud attenuation, that is, 1.2 dB (point B in Fig. 8a), the associated reflectivity Z_{10} at 10.7 cm is around 30 dBZ (1000 mm^6 m^{-3}) (Fig. 7b) and the relative errors on Z and R are, respectively, 0.13% and 0.10%. Although this relative error on R seems low, it has to be kept in mind that, in the present simulation, the radar wave propagation is only about 5.4 km into the cloud. For greater distances, cloud attenuation and, consequently, relative errors in measurements and physical property retrieval will be necessarily more important. At 0.86 cm (35 GHz), Lhermitte (1990) indicates that the Rayleigh approximation is acceptable until raindrop diameters of about 2.5 mm. Because in the model, raindrops larger than 2.5 mm are in lower concentration, the relation of Sekhon and Srivastava (1971) can be applied. In this context, the errors are about 4% and 3% on Z and R, respectively. In addition, taking into account the attenuation caused by the nimbostratus cloud, errors on Z and R are, respectively, 10% and 7.5% at 0.86 cm. Rain-rate retrieval will be thus more biased. This last consideration is crucial in a dual-radar method (or for radar network) since the target is rarely equidistant from all the radars. Hence, even if radars have the same wavelength, the retrieved reflectivity fields can be different because the radar wave propagation distances within the cloud, and subsequently attenuation, are not the same.

4. Simulations with other types and sizes of cumulus

In this section, the influence of the microphysical and geometrical cumulus characteristics on attenuation is investigated.

a. Influence of the maximum cumulus water content M_c^{max} on PICA

As $M_c^{\max}$ is a cloud microphysical characteristic, a question that naturally arises concerns the influence of $M_c^{\max}$ on PICA. Three other cumulus clouds have been thus modeled with the same thickness ($e = 2$ km) and shape factor ($s_f = 5$) but with various $M_c^{\max}$ values. Figure 12 displays the liquid water content vertical profile $M_c(z)$ for each considered cumulus, that is, an extreme congestus, a congestus, a mediocris, and a humilis ($M_c^{\max} = 3$, 1, 0.5, and 0.2 g m^{-3}, respectively). For each cumulus, cloud reflectivity fields (not shown) and PICA fields (not shown) have been computed. Table 1 summarizes the values obtained for the maximum PICA and the range of cloud reflectivity values.

As expected, the higher the $M_c^{\max}$ and, for a given $M_c^{\max}$, the lower the wavelength, the higher the maximum PICA. An interpolation in a least squares sense of these results has been performed in order to emphasize the influence of $M_c^{\max}$ on the maximum PICA. The results are given in Fig. 13 where the maximum cumulus attenuation is given as a function of $M_c^{\max}$. Moreover, the lower $M_c^{\max}$, the lower the cloud reflectivity: values between -5 dBZ (for the strongest cumulus) and -45 dBZ (for the weakest one) are frequently beyond the

TABLE 2. Same as in Table 1, except that the cumulus thickness is 1 km.

$M_c^{\max}$ (g m^{-3})		3	1	0.5	0.2
PICA maximum values (dB): $e = 1$ km and $s_f = 5$	$\lambda = 3.2$ cm	0.32	0.12	0.08	0.03
	$\lambda = 0.86$ cm	4.4	1.6	1	0.4
	$\lambda = 0.32$ cm	24	8	5	2
Cloud reflectivity at 10.7 cm (dBZ)		-25 to -5	-35 to -15	-40 to -20	-45 to -25

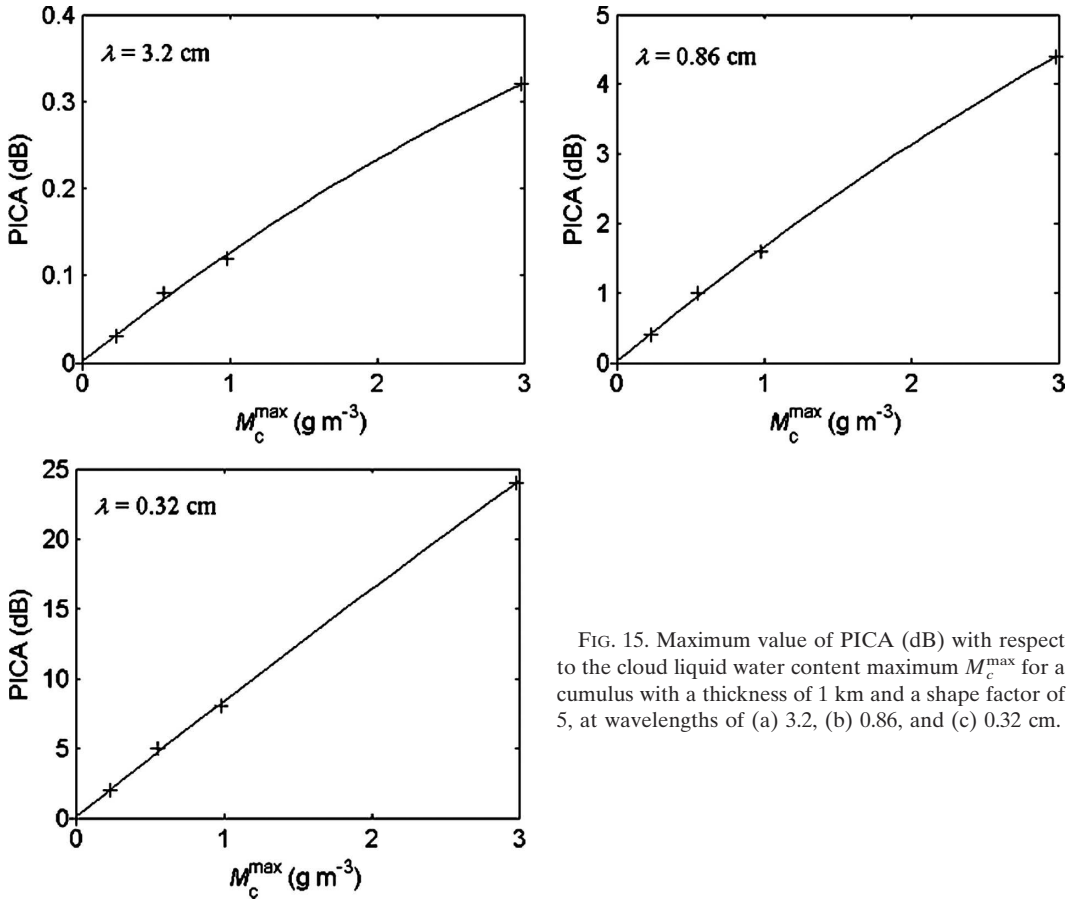

FIG. 15. Maximum value of PICA (dB) with respect to the cloud liquid water content maximum M_c^{max} for a cumulus with a thickness of 1 km and a shape factor of 5, at wavelengths of (a) 3.2, (b) 0.86, and (c) 0.32 cm.

sensitivity threshold of radars. So, cumulus clouds are hardly detectable.

b. Influence of the cloud thickness e on PICA

As cloud size also affects maximum cumulus attenuation, the simulations have been performed for smaller clouds characterized by a thickness of 1 km while keeping the shape factor constant ($s_f = 5$). Figure 14 displays the vertical profile of $M_c(z)$ and Table 2 sums up the results obtained. With respect to Table 1, the cloud reflectivity is not changed whereas, as expected, PICA maximum values are lower than for a cloud 2 km thick. As in section 4a, M_c^{max} is related to PICA for cumulus clouds 1 km thick (Fig. 15) by means of a least squares interpolation.

Combining the results presented in Tables 1 and 2, the dependence of the maximum PICA on the cumulus thickness e for a cloud whose shape factor is 5 can be presented. Figure 16 shows this dependency for various values of the liquid water M_c^{max} when observations are conducted at wavelengths of 3.2 (Fig. 16a), 0.86 (Fig. 16b), and 0.32 cm (Fig. 16c). As expected, for given values of the wavelength and M_c^{max}, the PICA maximum increases with e.

5. Conclusions and perspectives

To quantitatively estimate the cloud attenuation undergone by electromagnetic waves, two-dimensional radar observations of warm precipitating clouds are simulated. Simulations are performed at four different radar frequencies or wavelengths ($f = 3$ GHz, $\lambda \approx 10.7$ cm; $f = 10$ GHz, $\lambda \approx 3.2$ cm; $f = 35$ GHz, $\lambda \approx 0.86$ cm; $f = 94$ GHz, $\lambda \approx 0.32$ cm) from a simple model where cloud cells result from the superimposition of two distinct and independent parts: a liquid cloud and a liquid precipitation component. Each of these parts is defined through their respective liquid water content, which is supposed to be a spatial two-dimensional function derived from observations on cloud and precipitation (Borovikov 1963; Pruppacher and Klett 1997, section 2.1). The cloud droplet size distribution is then defined by considering a value of the cloud liquid water content and assuming a total cloud droplet concentration of

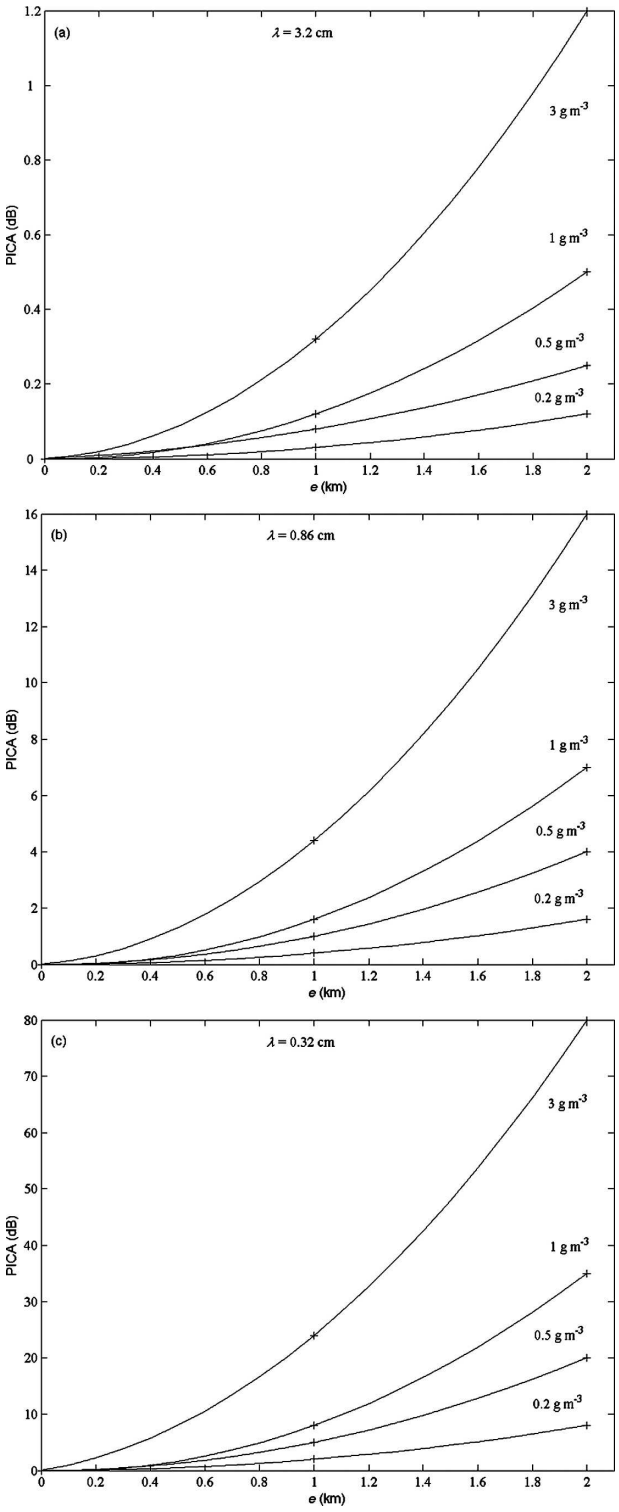

FIG. 16. Maximum value of PICA (dB) with respect to cumulus thickness e (km) according to cloud maximum liquid water content ($M_c^{\max}$ = 3, 1, 0.5, and 0.2 g m^{-3}); cloud shape factor is 5. Wavelengths of observations are (a) 3.2, (b) 0.86, and (c) 0.32 cm.

350 cm^{-3}. In a similar way, the raindrop size distribution is defined using a value of the rainwater content and a median drop diameter fixed to 2 mm. All the microphysical parameters computed in this study are deduced from observations, which ensures the reliability of our modeling conditions.

The first precipitating cell under consideration is a convective one, consisting of a vigorous cumulus congestus (maximum liquid water content is 3 g m^{-3}) associated with rain reaching the ground. The cloud thickness is 2 km and the shape factor is 5. Simulations that are conducted in order to observe the precipitation under the cumulus and to quantify its attenuation indicate that

- clouds have a relatively low reflectivity ranging from −25 to −5 dBZ and
- cloud attenuation can be very important at operational wavelength: for this extreme cumulus congestus, maximum cloud attenuation values of 1.2 dB at 3.2 cm, 16 dB at 0.86 cm, and 80 dB at 0.32 cm are obtained with respect to the 10.7-cm wavelength considered as the reference becomes weakly attenuated.

It is also demonstrated that these values are consistent with the meteorological target definition adopted, ensuring the reliability of the model.

From these results, it is concluded that cloud attenuation can highly affect radar observations and, consequently, can bias retrieved quantities as, for example, the precipitation rate R. The importance of cloud is also highlighted by noting that cloud reflectivities are low so that they are not easily detected.

Looking at the influence of a stratiform background, a nimbostratus associated with a drizzle field is superimposed on the convective cell, the nimbostratus being characterized by a maximum liquid water content of about 0.3 g m^{-3} and a thickness of 2 km. Nimbostratus-simulated reflectivities are lower than for the cumulus and range from −35 to −20 dBZ. Concerning attenuation, an offset of 0.3 dB at 3.2 cm, 4 dB at 0.86 cm, and 20 dB at 0.32 cm has to be added to the above attenuation values so that total cloud attenuations are 1.5 dB, 20 dB, and 100 dB, respectively.

Additional simulations on different types of cumulus clouds with various sizes are also performed. First, only the maximum water content is changed, defining three other cumulus clouds: a congestus, a mediocris, and a humilis with maximum cloud liquid water contents ($M_c^{\max}$) equal, respectively, to 1, 0.5, and 0.2 g m^{-3}. Cumulus sizes are then changed fixing the thickness e to 1 km and keeping constant the shape factor $s_f = 5$. First, the simulations show, as expected, that the lower $M_c^{\max}$,

the lower the cloud reflectivity; in addition, for a given wavelength, the higher $M_c^{\max}$ and e, the higher the cloud attenuation. Then, they give some orders of magnitude of the influence of $M_c^{\max}$ and e on the maximum cumulus attenuation in precipitation observations from airborne radar. The authors are aware that the model discussed in the present work concerns idealized examples, but it permits us to clearly illustrate the degradation of airborne radar reflectivity fields by cloud attenuation in the case of usual meteorological conditions. In addition, the model can be easily adapted to other more complex cases.

Research of methods to detect the presence of clouds and measure their attenuation is justified by the importance of the cloud component. Jameson (1995) has suggested an approach using a polarimetric radar for estimating cloud attenuation and cloud liquid water content in light and moderate rains. It is to be noted that only cloud droplet attenuation has been considered in this study, to quantify and illustrate the impact of warm clouds in radar observations and physical property retrievals. But, other sources of attenuation contribute to the degradation of the radar reflectivity, notably atmospheric gases (mainly water vapor and molecular oxygen). At 0.32 cm (94 GHz), gases produce attenuation close to 1 dB km^{-1} (Meneghini and Kozu 1990, p. 130 and Fig. 4.2 p. 131). Details concerning the microwave attenuation by atmospheric gases can be found in Liebe (1985). Further, drizzle, rain, and other hydrometeors also attenuate radar reflectivity. The quantification of their effects on radar wave should be the topic of further papers.

REFERENCES

Atlas, D., 1990: *Radar in Meteorology*. Amer. Meteor. Soc., 806 pp.

——, and F. H. Ludlam, 1961: Multi-wavelength radar reflectivity of hailstorms. *Quart. J. Roy. Meteor. Soc.,* **86,** 468–482.

Blanchard, D. C., 1953: Raindrop size distribution in Hawaiian rains. *J. Meteor.,* **10,** 457–473.

Borovikov, A. M., 1963: *Cloud Physics*. U.S. Dept. of Commerce, 392 pp.

Deirmendjian, D., 1969: *Electromagnetic Scattering on Spherical Polydispersions*. Elsevier, 290 pp.

Doviak, R. J., and D. Zrnić, 1993: *Doppler Radar and Weather Observations*. Academic Press, 562 pp.

Durden, S. L., E. Im, K. Li, W. Ricketts, A. Tanner, and W. Wilson, 1994: ARMAR: An Airborne Rain Mapping Radar. *J. Atmos. Oceanic Technol.,* **11,** 727–737.

Eccles, P. J., and E. A. Mueller, 1971: X-band attenuation and liquid water content estimation by dual-wavelength radar. *J. Appl. Meteor.,* **10,** 1252–1259.

——, and D. Atlas, 1973: A dual-wavelength radar hail detector. *J. Appl. Meteor.,* **12,** 847–854.

Féral, L., H. Sauvageot, and S. Soula, 2003: Hail detection using S-band and C-band radar reflectivity difference. *J. Atmos. Oceanic Technol.,* **20,** 233–248.

Gaussiat, N., H. Sauvageot, and A. J. Illingworth, 2003: Cloud liquid water and ice content retrieval by multiwavelength radar. *J. Atmos. Oceanic Technol.,* **20,** 1264–1275.

Glickman, T. S., Ed., 2000: *Glossary of Meteorology*. 2d ed. Amer. Meteor. Soc., 855 pp.

Goldhirsh, J., and I. Katz, 1974: Estimation of raindrop size distribution using multiple wavelength radar systems. *Radio Sci.,* **9,** 439–446.

Gossard, E. E., and R. G. Strauch, 1983: *Radar Observation of Clear Air and Clouds*. Elsevier, 280 pp.

Gosset, M., and H. Sauvageot, 1992: A dual-wavelength radar method for ice-water characterization in mixed-phase clouds. *J. Atmos. Oceanic Technol.,* **9,** 538–547.

Hildebrand, P. H., C. A. Walther, C. L. Frusch, J. Testud, and F. Baudin, 1994: The ELDORA/ASTRAIA airborne Doppler weather radar: Goals, design, and first field tests. *Proc. IEEE,* **82,** 1873–1890.

Hogan, R. J., A. Illingworth, and H. Sauvageot, 2000: Measuring crystal size in cirrus using 35- and 94- GHz radars. *J. Atmos. Oceanic Technol.,* **17,** 27–37.

Jameson, A. R., 1995: Using multiparameter radar to estimate the attenuation and water content of clouds. *J. Appl. Meteor.,* **34,** 2046–2059.

Khrgian, A. Kh., and I. P. Mazin, 1952: The size distribution of droplets in clouds. *Tr. Tsentr. Aerol. Obs.,* **7,** 56–61.

Lhermitte, R., 1990: Attenuation and scattering of millimeter wavelength radiation by clouds and precipitation. *J. Atmos. Oceanic Technol.,* **7,** 464–479.

Liebe, H., 1985: An updated model for millimeter wave propagation in moist air. *Radio Sci.,* **20,** 1069–1089.

Mason, B. J., 1971: *The Physics of Clouds*. The Pennsylvania State University Press, 481 pp.

Meneghini, R., and T. Kozu, 1990: *Spaceborne Weather Radar*. Artech House, 199 pp.

——, T. Iguchi, T. Kozu, L. Liao, K. Okamoto, J. A. Jones, and J. Kwiatkowski, 2000: Use of the surface reference technique for path attenuation estimates from the TRMM precipitation radar. *J. Appl. Meteor.,* **39,** 2053–2070.

Mie, G., 1908: Beiträge zur Optik trüber medien, speziell kolloidaler metallösungen. *Ann. Phys.,* **25,** 377–445.

Okita, T., 1958: Observations on vertical change of raindrop size distribution. Tohoku University Science Rep. 1, Geophysics Series 5, Vol. 10, 13 pp.

Oury, S., J. Testud, and V. Marécal, 1998: Estimate of precipitation from the dual-beam airborne radar in TOGA COARE. Part I: The *K–Z* relationships derived from stereo and quad-beam analysis. *J. Appl. Meteor.,* **38,** 156–174.

Pruppacher, H., and J. D. Klett, 1997: *Microphysics of Clouds and Precipitation*. Kluwer Academic, 943 pp.

Ray, P. S., 1972: Broadband complex refractive indices of ice and water. *Appl. Opt.,* **11,** 1836–1844.

Sauvageot, H., 1992: *Radar Meteorology*. Artech House, 366 pp.

——, and J. Omar, 1987: Radar reflectivity of cumulus clouds. *J. Atmos. Oceanic Technol.,* **4,** 264–272.

Schumacher, C., and R. A. Houze Jr., 2000: Comparison of radar data from the TRMM satellite and Kwajalein oceanic validation site. *J. Appl. Meteor.,* **39,** 2151–2164.

Sekhon, R. S., and R. C. Srivastava, 1971: Doppler radar observations of drop size distribution in thunderstorm. *J. Atmos. Sci.,* **28,** 983–994.

Squires, P., 1958: The microstructure and colloidal stability of warm clouds. *Tellus,* **10,** 256–271.

Srivastava, R. C., and J. Jameson, 1977: Radar detection of hail. *Hail: A Review of Hail Science and Hail Suppression, Meteor. Monogr.,* No. 38, Amer. Meteor. Soc., 269–277.

——, and L. Tian, 1996: Measurement of attenuation by a dual-radar method: Concept and error analyses. *J. Atmos. Oceanic Technol.,* **13,** 937–947.

Stratton, J. A., 1941: *Electromagnetic Theory*. McGraw-Hill, 702 pp.

Testud, J., and P. Amayenc, 1989: Stereoradar meteorology: A promising technique for observation of precipitation from a mobile platform. *J. Atmos. Oceanic Technol.,* **6,** 89–108.

Ulbrich, C. W., 1983: Natural variations in the analytical form of the raindrop size distribution. *J. Climate Appl. Meteor.,* **22,** 1764–1775.

Vivekanandan, J. E., M. Brooks, M. K. Politovich, and G. Zhang, 1999: Retrieval of atmospheric liquid and ice characteristics using dual-wavelength radar observations. *IEEE Trans. Geosci. Remote Sens.,* **37,** 2325–2333.

Vulfson, N. I., A. G. Laktinov, and V. I. Skatskii, 1973: Cumuli structure at various stages of development. *J. Appl. Meteor.,* **22,** 664–670.

Warner, J., 1955: The water content of cumuliform cloud. *Tellus,* **7,** 449–457.

——, 1969: The microstructure of cumulus cloud. Part I. General features of the droplet size spectrum. *J. Atmos. Sci.,* **26,** 1049–1059.

——, 1970: The microstructure of cumulus cloud. Part III. The nature of the updraft. *J. Atmos. Sci.,* **27,** 682–688.

Yeh, H.-Y. M., N. Prasad, R. Meneghini, W.-K. Tao, J. A. Jones, and R. F. Adler, 1995: Cloud model–based simulation of spaceborne radar observations. *J. Appl. Meteor.,* **34,** 175–197.

Zaitsev, V. A., 1950: Water content and distribution of drops in cumulus clouds. *Gla. Geofiz. Obs. Tr.,* **19,** 122–132.